Modeling of modern MOSFETs with strain

V. Sverdlov · O. Baumgartner · T. Windbacher · S. Selberherr

Abstract We review modeling techniques used to compute strain induced performance enhancement of modern MOS-FETs. While p-channel MOSFETs were intensively studied, electron transport in strained structures received surprisingly little attention. A rigorous analysis of the subband structure in thin silicon films under stress is performed. Calculated subband effective masses are shown to strongly depend on shear strain and film thickness. A decrease of the transport effective mass under tensile stress in [110] direction and an additional splitting between the unprimed subbands with the same quantum number guarantees a mobility enhancement even in ultra-thin (001) silicon films. This increase of mobility and drive current combined with the improved channel control makes multi-gate MOSFETs based on thin films or silicon fins preeminent candidates for the 22 nm technology node and beyond.

Keywords MOSFETs modeling · Shear strain · Two-band k·p model for conduction band · Valley splitting · Mobility and current enhancement

V. Sverdlov (✉) · O. Baumgartner · T. Windbacher · S. Selberherr
Institute for Microelectronics, TU Wien, Gußhausstraße 27-29, 1040 Vienna, Austria
e-mail: sverdlov@iue.tuwien.ac.at
url: http://iue.tuwien.ac.at

O. Baumgartner
e-mail: baumgartner@iue.tuwien.ac.at

T. Windbacher
e-mail: windbacher@iue.tuwien.ac.at

S. Selberherr
e-mail: selberherr@iue.tuwien.ac.at

1 Introduction

The rapid increase in computational power and speed of integrated circuits is supported by the aggressive size reduction of semiconductor devices. Downscaling of MOSFETs as institutionalized by Moore's law is successfully continuing because of innovative changes in the technological processes and the introduction of new materials. Until recently, the main method of increasing complementary metal-oxide semiconductors (CMOS) transistor performance was based on geometrical scaling, which has led to an enormous success in increasing the speed and functionality of electronic devices. Although a possibility to build a MOS-FET with a gate length as short as 6 nm has been demonstrated [1], the semiconductor industry is facing increasing difficulties with ongoing scaling continuing. Among them are the short channel effects and the high power dissipation for small transistors, and the high gate leakage current for very thin gate dielectrics. Already now, for an oxide thickness of approximately 1.5 nm, gate leakage makes it difficult to maintain a sufficiently high I_{on}/I_{off} ratio, which does not degrade MOSFET performance. Rising costs of chip manufacturing are making further scaling increasingly more difficult: the feasibility of fabrication cannot be easily guaranteed, and maintaining performance and reliability becomes a severe issue. With scaling apparently approaching its fundamental limits, the semiconductor industry is facing critical challenges. New engineering solutions and innovative techniques are required to improve CMOS device performance. Strain-induced mobility enhancement is the most attractive way to increase the device speed and will certainly take a key position among other technological changes for the next technology generations. The 32 nm MOSFET process technology recently developed by Intel [2] employs advanced third generation strain engineering techniques. Apart from

strain, the 32 nm MOSFET process technology involves new hafnium-based high-k dielectric/metal gates first introduced for the 45 nm technology node [3], which represented a major change in the technological process since the invention of MOSFETs. Although alternative channel materials with a mobility higher than in silicon were already investigated [4, 5], it is commonly believed that strained silicon will be the main channel material also for MOSFETs beyond the 32 nm technology node.

In addition, new device architectures based on multi-gate structures with better electrostatic channel control and reduced short channel effects will be developed. A multi-gate MOSFET architecture is expected to be introduced for the 22 nm technology node. Combined with a high-k dielectric/metal gate technology and strain engineering, a multigate MOSFET appears to be the ultimate device for high-speed operation with excellent channel control, reduced leakage currents, and low power budget.

In the following we shortly review stress techniques commonly used to enhance transport in CMOS FETs. We summarize the results for the relatively well understood mobility enhancement in p-channel MOSFETs. Then we briefly review the main ideas behind the two-band k·p model to describe the conduction band of silicon and analyze the subband structure in (001) ultra-thin films, calculating the subband quantization energies and effective masses. The subband dispersions are embedded into a subband Monte Carlo code in order to enable the computation of the low-field mobility. Results of the maximum current enhancement in a MOSFET at its ultimate scaling limit are analyzed.

2 Strain engineering techniques

Strain engineering technologies are based on physically stretching or/and compressing the silicon crystal lattice. The influence of strain on the intrinsic mobility of silicon was first investigated in the early 1950's [6, 7] and was revived in the beginning of the 1990's [8]. A number of strain technologies have been developed. The techniques to introduce stress can be classified in two categories. Stress can be introduced in the whole substrate wafer globally. Global stress in silicon can by typically created by epitaxially growing silicon on (001) oriented SiGe substrate. Due to the crystal lattice mismatch between silicon and SiGe, silicon is symmetrically stretched along the directions [100] and [010]. In 1992 it was demonstrated that n-channel MOSFETs on a strained silicon substrate exhibit a 70% higher effective mobility [9, 10]. Global strain techniques are not restricted to bulk-CMOS technology and may be integrated into silicon-on-insulator wafers by layer transfer and wafer bonding techniques. Benefits of performance for n-channel MOSFETs with ultra-thin strained silicon on SiGe-on-insulator substrate [11, 12]

or strained silicon directly on insulator were successfully demonstrated with current drive enhancements of 20–25% reported [13, 14].

However, the global stress techniques did not receive so far a broad commercial appreciation and recognition. The reason is the decrease of the hole mobility in p-channel MOSFETs in biaxially strained silicon grown on (001) SiGe substrate for up to 20% germanium concentration [15, 16], regardless of the large hole mobility enhancement anticipated in the bulk [17]. Since in unstrained silicon the mobility of holes is usually lower than the electron mobility, it is beneficiary to enhance the mobility of holes for CMOS applications, where similar on-currents are required in n-channel and p-channel MOSFETs. It turns out that for (001) oriented wafers the hole mobility is enhanced along the [110] direction by compressive stress, while the electron mobility in [110] direction is enhanced by tensile stress. Thus, the semiconductor industry has chosen a path on which stress is delivered to *each* n-channel and p-channel MOSFET *independently*. In these techniques stress is created locally by additional process steps [18–22]. A direct way to introduce stress in a MOSFET's channel is to fill the source and drain regions with SiGe [23, 24] for p-channel MOSFETs and with SiC for n-channel MOSFTEs [25, 26]. Additional uniaxial stress is often introduced by growing compressive or tensile capping layers [27–29]. The advantage of local stress techniques is that they can be combined [30] and superimposed [31] on the same wafer.

Stress is not the only option to improve mobility. An approach called the hybrid orientation technique is based on the optimization of carrier mobility in silicon inversion layers depending on the crystal orientation and the current flow direction for both n-channel and p-channel MOSFETs. The hole mobility is 2.5 times higher on (110) oriented substrate as compared to a standard (001) wafer surface [16]. The hybrid orientation technique is compatible with existing state-of-the-art strain engineering processes and is very promising for p-channel MOSFET performance enhancement. A comprehensive analysis of transport in multi-gate MOSFETs under general stress conditions is required for understanding the enhancement of device performance.

3 Modeling of p-channel MOSFETs

Mobility enhancement in p-channel MOSFETs was intensively studied theoretically and good understanding was achieved. Due to the complex valence band structure in silicon, the consideration must be based on the 6-band k·p model [32], which takes into account the bands of heavy and light holes and the split-off band due to spin–orbit interaction. When stress is applied, splitting between the heavy and light hole bands and/or effective mass change appears.

Strain can be easily incorporated into the formalism of the k·p method [33]. Due to the band splitting re-population between the heavy and light holes bands is expected. Since the heavy and light holes have different conductivity masses, which may depend on the stress value, the change in their relative population introduces the mobility change. Because of the change of the density of states and band splitting, scattering also depends strongly on strain. In general, due to the complexity of the band structure, an accurate solution of the Boltzmann equation is needed in order to evaluate the mobility enhancement. Bulk in-plane and out-of-plane hole mobility in biaxially strained or, equivalently, uniaxially along [001] direction strained silicon was investigated in detail [17]. Recently, hole mobility in the bulk under uniaxial [110] stress was modeled [15, 34].

The hole mobility in inversion layers for general strain conditions was carefully studied for several important substrate orientations [15, 16, 35]. Mobility on a (110) unstrained surface is found roughly 2.5 times higher than on a standard (001) wafer, in agreement with earlier measurements [36]. It was found that biaxial tensile stress decreases mobility on a (001) surface [15, 16]. At high stress the largest surface mobility enhancement factor was predicted for (001) oriented wafers, when transport is along the [110] direction under compressive uniaxial stress [16]. However, the maximum value of mobility at saturation was found along the [110] direction under uniaxial compressive stress at (001) and (1-10) surfaces [16]. Recently, a nearly three-fold on-current enhancement due to [110] compressive stress was predicted in strained double-gate structures with the help of a deterministic multi-subband device simulator [37].

4 Challenges of n-channel MOSFET modeling

The conduction band in silicon consists of six equivalent valleys with their energy minima located close to the corresponding X-points of the first Brillouin zone. Within the usually used parabolic approximation each valley is characterized by two transversal and one longitudinal effective mass [38]. At higher energy a non-parabolic isotropic correction must be included to reproduce the density of states correctly [38].

The change in the conduction band of silicon under biaxial stress is well understood [17, 39]. Biaxial stress causes splitting between the six equivalent valleys. The splitting prompts re-populations between the valleys and also reduces inter-valley scattering. These effects lead to a substantial bulk mobility enhancement due to a biaxial tensile stress. Mobility in biaxially stressed silicon both in the bulk [17] and in the electron inversion layers [40, 41] was carefully investigated.

The application of local stress techniques results in creating uniaxially stressed silicon in the channel. Since the usual channel orientation on a (001) wafer is along [110] direction, the local stress is typically aligned with the [110] axis. Although already being used in mass production, the stress along [110] direction has received surprisingly little attention within the research community. Only recently a systematic experimental study of the mobility modification due to [110] stress was performed [42].

It was shown that the electron mobility data on (001) substrate under [110] uniaxial stress is consistent with the conductivity mass depending on the stress value, in contrast to biaxially stressed silicon, where the conductivity mass was shown to be virtually independent of the stress value [17]. This effective mass dependence cannot be recovered within the effective mass approximation, and a generalization of the conduction band description in uniaxially stressed silicon is needed.

Another shortcoming of the effective mass approximation for the conduction band becomes apparent in structures with thin silicon bodies. Confining carriers within thin films reduces the channel dimension in transversal direction, which further improves gate channel control. The quantization energy in ultra-thin silicon films may reach hundreds of meV. The parabolic band approximation usually employed for subband structure calculations of confined electrons in silicon inversion layers becomes insufficient in ultra-thin films. A recent study of subband energies and transport in (001) and (110) oriented thin films reveals that even a non-parabolic isotropic dispersion relation is not sufficient to describe experimental data, and a direction-dependent anisotropic non-parabolicity must be introduced [43].

In order to overcome these difficulties, the effective mass approximation usually applied for the conduction band must be generalized. An approach based on the full band structure computed with the empirical pseudo-potential method (EPM) [44] is promising and has been recently generalized to include strain and spin–orbit interaction [45]. Although it uses a realistic band structure, the method is computationally demanding and needs to be improved to include the self-consistent solution of Poisson equation.

Another approach is based on the k·p theory. Recently, a 30-band k·p method [46] was employed to investigate subbands in thin films. The method gives an accuracy comparable with the 6-band k·p method for the valence band. Since the method is developed around the Γ-symmetry point, it requires all 30 bands to obtain results for the conduction band minima located close to the edge of the first Brillouin zone.

The two-band k·p model [33, 47–49] is developed in the vicinity of the X-point and thus provides a natural framework to compute the subband structure, in particular the dependences of the electron effective masses on shear strain

and thickness, in thin films. In the case of a square potential well with infinite walls, which is a good approximation for the confining potential in ultra-thin films, the subband structure can be obtained analytically [50]. This allows for an analysis of subband energies, effective masses, non-parabolicity, and the low-field mobility on film thickness for arbitrary stress conditions.

The peculiarity of [110] uniaxial stress is that it produces an off-diagonal element ε_{xy} of the strain tensor and results in a shear distortion of the crystal. Under shear deformation a significant change in the band structure appears. Namely, due to non-zero values of the shear deformation potential D, the degeneracy between the two lowest conduction bands at the X-points of the Brillouin zone along the [001] axis is lifted [33]. Thus, for non-zero values of ε_{xy} an additional energy splitting $\Delta E_X = 2|D\varepsilon_{xy}|$ between the two conduction bands appears at the X-point. Due to this splitting, the effective masses in the valleys along [001] direction are substantially modified and become functions of the shear stress value. It is worth noticing that uniaxial stress along [001] direction, which produces a biaxially stressed (001) substrate, does not contain the shear strain component. Therefore, the influence of [110] uniaxial stress on the band structure and transport must be carefully investigated.

In the following we briefly review the main ideas behind the two-band k·p model for a valley in the conduction band of silicon. Then we shortly analyze the unprimed subband structure in (001) ultra-thin films, obtaining analytical expressions for the effective masses and non-parabolicity parameter. With these parameters the non-parabolic subband approximations for the subband dispersions are constructed. The non-parabolic subband dispersions are embedded into a subband Monte Carlo code in order to enable the computation of the low-field mobility. Results of the mobility enhancement calculations are finally analyzed.

5 Conduction band in silicon

5.1 Two-band k·p Hamiltonian

The subband structure in a confined system must be based on accurate bulk bands including strain, where various options are available. The conduction band dispersions computed with several methods in [100] and [110] directions are compared in Fig. 1a. The method based on non-local empirical pseudo-potentials from [39, 48] is the most accurate one as compared to DFT band structure results obtained with VASP [51–54]. The sp^{3}d^{5}s* tight-binding model with parameters from [55] does not reproduce the anisotropy of the conduction band correctly. In addition, an accurate calibration of the parameters of the sp^{3}d^{5}s* model to describe the modification of the conduction band in strained silicon was performed only recently [56, 57].

The k·p theory is a well established method to describe the band structure analytically. As illustrated in Fig. 1a, the k·p method reproduces the band structure accurately at energies below 0.6 eV, which is sufficient to describe the subband structure and transport properties of advanced MOSFETs. From symmetry considerations the two-band k·p Hamiltonian of a [001] valley in the vicinity of the X-point of the Brillouin zone in silicon must be in the form [33]:

$$H = \left(\frac{\hbar^2 k_z^2}{2m_l} + \frac{\hbar^2 (k_x^2 + k_y^2)}{2m_t} \right) I + \left(D\varepsilon_{xy} - \frac{\hbar^2 k_x k_y}{M} \right) \sigma_z$$
$$+ \frac{\hbar^2 k_z k_0}{m_l} \sigma_x, \tag{1}$$

where $\sigma_{x,z}$ are the Pauli matrices, I is the 2×2 unity matrix, m_t and m_l are the transversal and the longitudinal effective masses, $k_0 = 0.15 \times 2\pi/a$ is the position of the valley minimum relative to the X-point in unstrained silicon, ε_{xy} denotes the shear strain component, $M^{-1} \approx m_t^{-1} - m_0^{-1}$, and $D = 14$ eV is the shear strain deformation potential [33, 47–49]. The two-band Hamiltonian results in the following dispersion relations [33]:

$$E = \frac{\hbar^2 k_z^2}{2m_l} + \frac{\hbar^2 (k_x^2 + k_y^2)}{2m_t} \pm \sqrt{ \left(\frac{\hbar^2 k_z k_0}{m_l} \right)^2 + \delta^2 }, \tag{2}$$

where the negative sign corresponds to the lowest conduction band,

$$\delta^2 = (D\varepsilon_{xy} - \hbar^2 k_x k_y/M)^2. \tag{3}$$

All moments as well as energies in (2) are counted from the X-point of the Brillouin zone. The classical parabolic approximation is obtained from (2), when coupling between the two conduction bands described by the parameter δ is neglected. The coupling between the bands is small, when the wave vectors $|k_x|, |k_y| \ll k_0 (M/m_l)^{1/2}$ and shear strain $\varepsilon_{xy} = 0$. Due to band coupling the dispersion relations (2) become non-parabolic, if the shear strain component is non-zero, and/or at higher energies. In order to check the accuracy of (2) we have carried out numerical band structure calculations using the EPM with parameters from [39, 48]. Excellent agreement between the two-band k·p model (1) and the EPM results was found up to an energy of 0.6 eV. Equation (2) is valid in a larger range of energies compared to a parabolic dispersion relation with isotropic non-parabolic correction and can be used to determine the subband structure in thin silicon films.

5.2 Valley shift due to shear strain

It follows from (2) that the position of the conduction band minimum located at a distance k_0 from the X-point in unstrained silicon moves closer to the X-point for non-zero
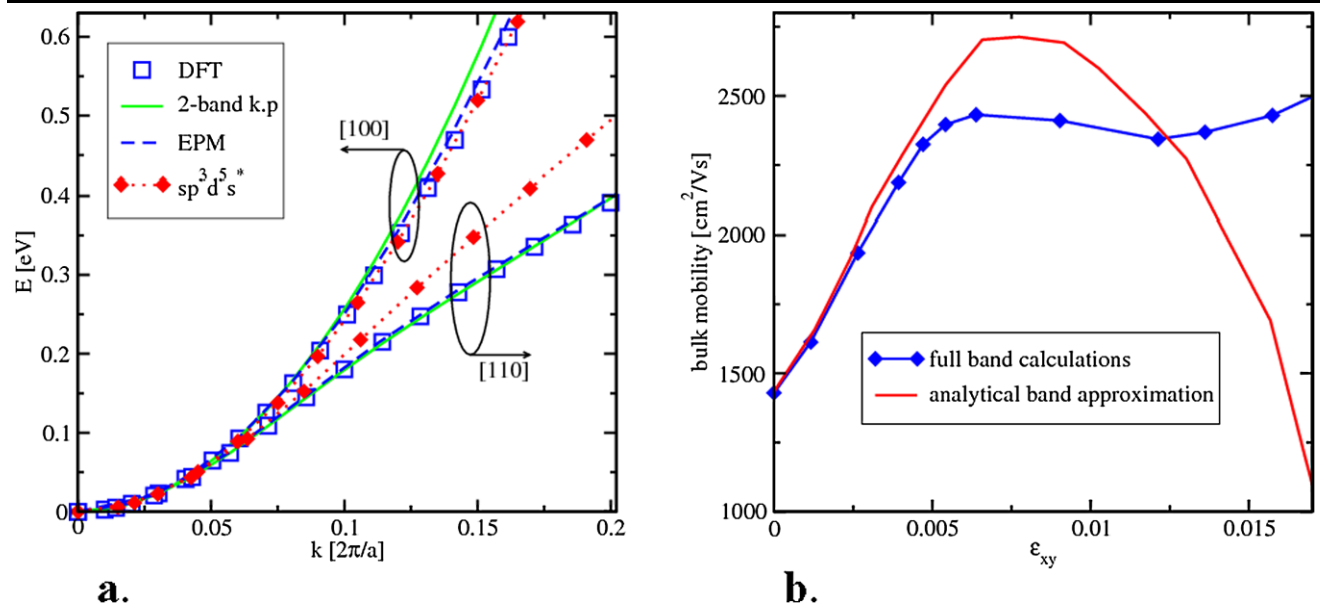
a.

Fig. 1 a. Comparison of bulk dispersions close to the minimum of the [001] valleys of the conduction band in [100] and [110] directions. The DFT [51–54] and EPM [39, 48] results are similar, while the sp^{3}d^{5}s* tight-binding model [55] underestimates anisotropy sig-

nificantly. **b.** Bulk mobility computed by accounting for the full-band structure (*symbols*) and approximated with non-parabolic dispersion of six valleys (*solid line*)

shear strain. Introducing dimensionless strain

$$\eta = m_l \delta / \hbar^2 k_0^2,$$

one finds for the position of the minimum [48, 49]:

$$k_{\min}/k_0 = \sqrt{1 - \eta^2}. \qquad (4a)$$

At the same time the minimum moves down in energy:

$$\Delta E_{\min} = -\eta^2 \Delta/4, \quad |\eta| \leq 1, \qquad (4b)$$

where $\Delta = 2\hbar^2 k_0^2 / m_l$ is the gap between the two conduction bands at the minimum k_0. For $|\eta| \geq 1$ the conduction band minimum stays exactly at the X-point, resulting in the following energy dependence:

$$\Delta E_{\min} = -(2|\eta| - 1)\Delta/4, \quad |\eta| \geq 1. \qquad (4c)$$

5.3 Effective masses

Shear strain ε_{xy} modifies the effective masses of the [001] valleys. The transversal mass m_t acquires two different values along $(+)$ and across $(-)$ tensile stress direction [48, 49]:

$$m_t(\eta)/m_t = [1 \pm |\eta| m_t/M]^{-1}, \quad |\eta| \leq 1; \qquad (5a)$$

$$m_t(\eta)/m_t = [1 \pm m_t/M]^{-1}, \qquad |\eta| \geq 1. \qquad (5b)$$

The longitudinal mass m_l is expressed as

$$m_l(\eta)/m_l = [1 \pm \eta^2]^{-1}, \qquad |\eta| \leq 1; \qquad (6a)$$

$$m_l(\eta)/m_l = [1 \pm |\eta|^{-1}]^{-1}, \quad |\eta| \geq 1. \qquad (6b)$$

5.4 Non-parabolicity

From the two-band Hamiltonian the value of the non-parabolicity parameter is $\alpha_0 \approx 0.6$ eV^{-1} [13]. It is close to the phenomenological value $\alpha_0 = 0.5$ eV^{-1} routinely used in calculations. Strain induced modification of the conduction band effective masses affects the non-parabolicity parameter α of the [001] valleys.

The expression for the density-of-states can be written in the form [14]

$$D(E) = \int \frac{dk_x dk_y}{(2\pi)^2} \delta(E - E_n(k_x, k_y))$$

$$= \frac{\sqrt{m_-(\eta)m_+(\eta)}}{(2\pi)^2} \int_{E=\text{const}} d\varphi \frac{1}{2} \frac{\partial \zeta^2(E, \varphi)}{\partial E}, \qquad (7a)$$

where $\zeta^2(E, \varphi) = k_-^2/m_t^-(\eta) + k_+^2/m_t^+(\eta)$ is determined by the expression:

$$E = \frac{\zeta^2}{2} - \frac{\hbar^2 m_l}{8M^2 k_0^2 |1 - q_n^2|}(m_- \cos^2 \varphi - m_+ \sin^2 \varphi)^2 \zeta^4. \qquad (7b)$$

Substituting (7b) into (7a) and assuming the energy E close to the valley minimum so that $\alpha E \ll 1$, we obtain the fol-

lowing expression for the non-parabolicity parameter ratio:

$$\alpha = \alpha_0 \frac{1 + 2(m_t\eta/M)^2}{(1 - (m_t\eta/M)^2)^2}.$$

The relative increase of α resulting in an increased density of states and scattering are responsible for a weaker mobility enhancement (Fig. 1b) as compared to the mobility obtained with strain-independent α_0. However, for a stress larger than 3 GPa ($\eta \geq 0.5$) the energy difference from the minimum to the value at the X-point becomes smaller than kT, and a full-band description is required for accurate mobility calculations [15].

6 Subbands in (001) silicon films

6.1 Dispersion equations for unprimed subbands

For [001] silicon films the confinement potential gives an additional contribution $U(z)I$ to the Hamiltonian (1). In the effective mass approximation described by (1) with the coefficient in front of σ_x set to zero, the confining potential $U(z)$ is known to quantize the six equivalent valleys of the conduction band of bulk silicon into the four-fold degenerate primed and the two-fold degenerate unprimed subband ladder [38]. In ultra-thin films the unprimed ladder is predominantly occupied. In order to analyze the subbands, we approximate the confining potential of an ultra-thin silicon film by a square well potential with infinite potential walls. Generalization to include a self-consistent potential is straightforward though numerically involved [58].

Because of the two-band Hamiltonian, the wave function Ψ is a spinor with the two components $|0\rangle$ and $|1\rangle$. For a wave function with space dependence in the form $\exp(ik_z z)$ the coefficients A_0 and A_1 of the spinor components are related via the equation $H\Psi = E(k_z)\Psi$. For a particular energy E there exist four solutions k_i ($i = 1, \ldots, 4$) for k_z of the dispersion relation (2), so the spatial dependence of a spinor component is of the form $\sum_{i=1}^{4} A_\alpha^i \exp(ik_i z)$. The four coefficients are determined by the boundary conditions that both spinor components are zero at the two film interfaces. This leads to the following dispersion equations [59]:

$$\tan\left(k_1\frac{k_0 t}{2}\right) = \frac{k_2}{\sqrt{k_2^2 + \eta^2} \pm \eta} \frac{\sqrt{k_1^2 + \eta^2} \pm \eta}{k_1} \tan\left(k_2\frac{k_0 t}{2}\right),$$
$$(8)$$

where $\eta = m_l|\delta|/(\hbar k_0)^2$. If the value of

$$k_2 = \sqrt{k_1^2 + 4 - 4\sqrt{k_1^2 + \eta^2}} \qquad (9)$$

becomes imaginary at high η values, the trigonometric functions in (8) are replaced by the hyperbolic ones. Special care must be taken to choose the correct branch of $\sqrt{k_2^2 + \eta^2}$ in (9): the sign of $\sqrt{k_2^2 + \eta^2}$ must be alternated after the argument becomes zero. Introducing $y_n = (k_1 - k_2)/2$, (8) can be written in the form [59]:

$$\sin(y_n k_0 t) = \pm \frac{\eta y_n \sin\left(\sqrt{\frac{1-\eta^2-y_n^2}{1-y_n^2}} k_0 t\right)}{\sqrt{(1 - y_n^2)(1 - \eta^2 - y_n^2)}}. \quad (10)$$

If y_n is known, the value of k_1 and k_2 are found from the relations $k_{1,2} = (x_n \pm y_n)$, where

$$x_n = \sqrt{1 - \frac{\eta^2}{1 - y_n^2}}.$$

After substituting the values k_1 or k_2 (2) the subband energy relative to the unstrained bulk band minimum energy can be written as

$$E_n = \frac{\Delta}{4}\left(\left[\sqrt{(x_n \pm y_n)^2 + \eta^2} - 1\right]^2 - \eta^2\right).$$

6.2 Subband structure in thick films

We solve (10) by perturbation techniques. For small η the right-hand side in (10) can be ignored. The subband relations are found from the condition

$$y_n^0 = q_n \equiv \pi n/(k_0 t). \quad (11)$$

This results in the following approximate dispersion relation for unprimed subbands (50):

$$E_n(k_x, k_y) = E_n^0(k_x, k_y) - \Delta\eta^2/[4|1 - q_n^2|]. \quad (12)$$

Here the energies are counted from the conduction band minimum in the unstrained crystal, and E_n^0 is the subband dispersion relation for parabolic bands:
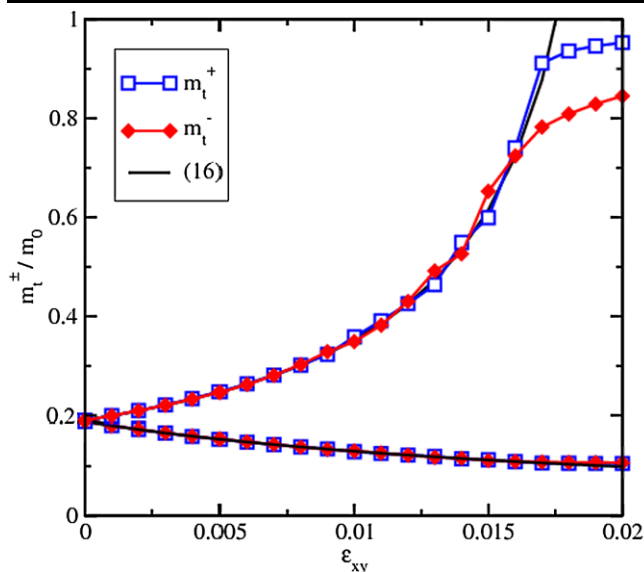
$$E_n^0(k_x, k_y) = \frac{\hbar^2\pi^2 n^2}{2m_l t^2} + \frac{\hbar^2(k_x^2 + k_y^2)}{2m_t} - \frac{\hbar^2 k_0^2}{2m_l}.$$

Equation (12) is valid when

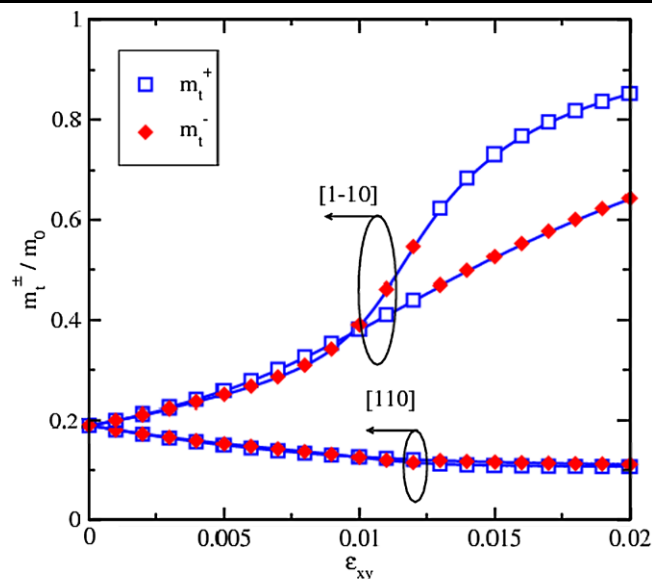$$(1 - q_n^2)^2 \gg \delta^2 m_l^2/\hbar^4 k_0^4. \quad (13)$$

Equation (12) describes the subband quantization energy correction due to strain with respect to the valley minimum

$$\Delta E_n(\eta) = -\frac{\hbar^2\pi^2 n^2}{2m_l t^2} \frac{\eta^2}{|1 - q_n^2|}, \quad (14)$$

a.

Fig. 2 Effective masses of the two ground subbands. The *symbols* are results obtained by numerical solution of the two-band Hamiltonian (1): **a**. $t = 10.86$ nm; *solid lines* are according to (16);

b.

b. $t = 5.43$ nm; *solid lines* are obtained by numerically differentiating subband dispersions obtained from (8)

which is obtained after taking into account the strain-induced valley minimum energy shift $\Delta E_{\min}$. Equation (14) can be absorbed into the quantization energy $\frac{\hbar^2 \pi^2 n^2}{2 m_l t^2}$ by introducing the longitudinal mass m_l depending on strain η and thickness t:

$$m_l(\eta, q_n) = \frac{m_l}{1 - \eta^2 / |1 - q_n^2|}. \tag{15}$$

Equation (12) also describes dependencies of the transversal masses on strain η, the film thickness t, and subband number n:

$$m_t^{\mp}(\eta, q_n) = m_t \left(1 \pm \eta \frac{m_t}{M} \frac{1}{|1 - q_n^2|} \right)^{-1}. \tag{16}$$

Here m_t^- is the effective mass along the direction [110] of tensile stress. Equation (16) demonstrates that the effective mass in films depends not only on strain but also on film thickness.

6.3 Numerical solutions

In order to analyze the subband structure in (001) oriented thin silicon films we first approximate the film potential by the square well potential with infinite potential walls. Although not exact, this is a good approximation for thin films. To obtain the values for the subband splitting and effective masses for an arbitrary strain value, (8) can be solved numerically. Alternatively, the eigenvalues can be found by resolving the equations obtained by discretizing the Hamiltonian (1) with $k_z = -i \frac{d}{dz}$ and the confinement potential

$IU(z)$ added. The latter method is more general, because it allows the inclusion of a confinement potential of arbitrary form making self-consistent calculations possible.

Both numerical routines were implemented, and equivalent results were obtained by the two methods in case of a square well potential with infinite walls.

6.3.1 Effective masses of unprimed subbands

We compare (16) (lines) with the results of the numerical solution of the two-band k·p model Hamiltonian (symbols) in a film with a thickness $t = 10.86$ nm for the ground subbands ($n = 1$) and find a good agreement shown in Fig. 2a. However, when the film thickness decreases a substantial discrepancy between (16) and the numerical solution appears, especially at high values of strain, as shown in Fig. 2b. Figure 3a demonstrates the effective masses on strain of the two ground subbands in ultra-thin silicon films. Interestingly, the effective masses in relaxed ultra-thin films become different along [110] or [1-10] directions. Their dependence on the film thickness is displayed in Fig. 3b. Although the subbands are characterized by the effective masses, due to symmetry restrictions their subband dispersions, however, are not parabolic as demonstrated in Fig. 4a and Fig. 4b. The subband which for given k_x, k_y has a lower energy has the equi-energies in the form of a unification of the two ellipses with the effective masses m_1, m_2, while the equi-energies for the higher subband are described by intersection of the same ellipses.
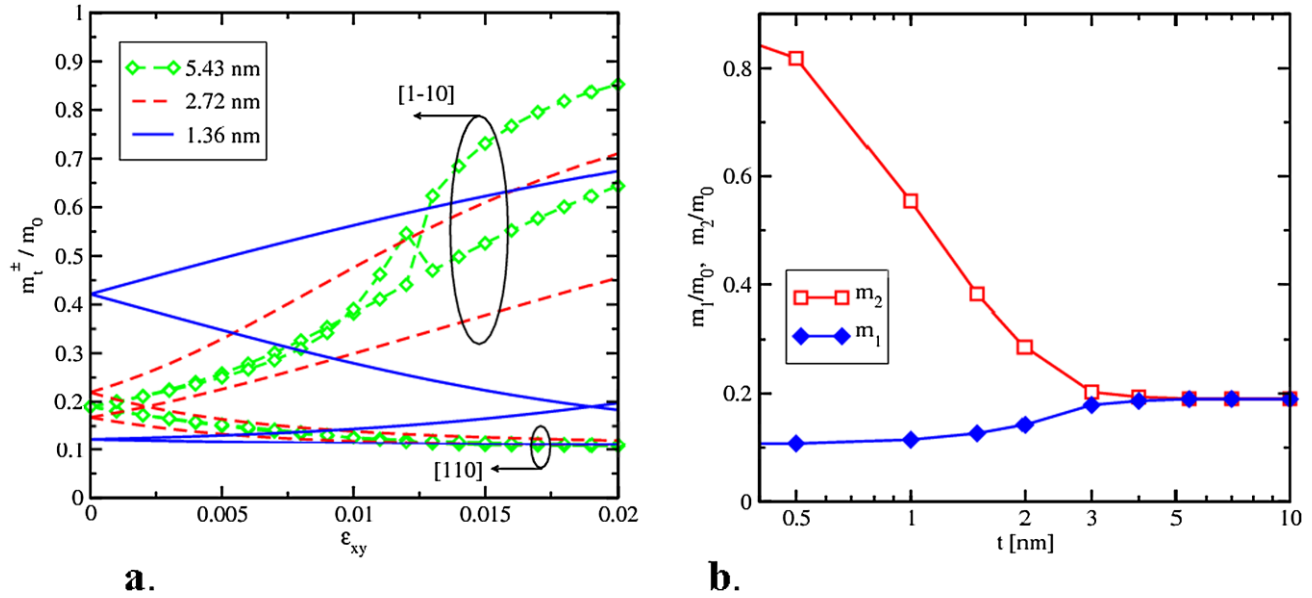
Fig. 3 **a**. Effective masses of the two ground subbands. In ultra-thin films the effective masses of the two ground subbands are different even without stress. **b**. The thickness dependence of the effective masses in unstrained films of the two lowest unprimed subbands
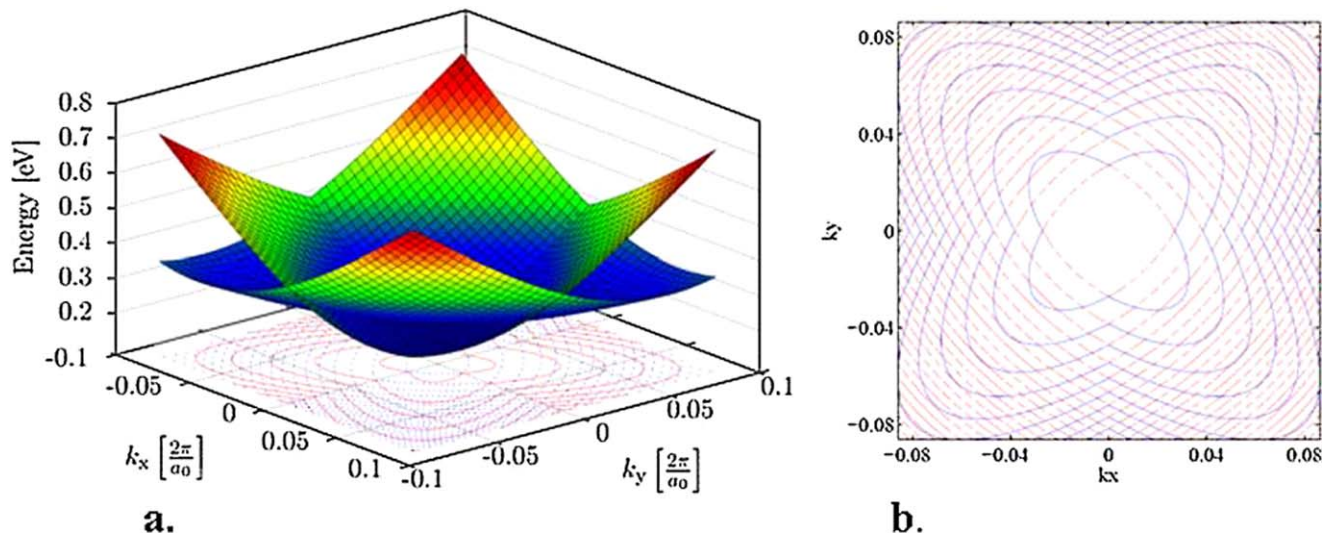

Fig. 4 (Color online) Dispersions of the two ground subbands for a film thickness of 1.36 nm: **a**. Without strain the subbands are degenerate at the minimum. The lower subband dispersion is *dark blue* and described by the unification of the two ellipses with different masses (18), while the second subband is described by their intersection. **b**. Contour plot of the ground subbands

This discrepancy between (16) and numerical results is caused by the growing value of the right-hand side in (10), which cannot be ignored in thin films. The right-hand side of (10) is due to an interaction between the two conduction bands in (1). The two bands have their minima at $k_z = \pm k_0$ with respect to the corresponding X-point. The coupling between the bands can be viewed as an interaction between the valleys. As one sees from (10), the interaction between the valleys is due to the term $\eta \neq 0$. This is exactly the term

which causes the non-parabolicity of the bulk bands as it can bee seen from (2).

Substituting (11) into the right-hand side of (10) and solving (10) for small strain η one obtains the following dispersion relation for the unprimed subbands n:

$$E_n^\pm = \frac{\hbar^2}{2m_l}\left(\frac{\pi n}{t}\right)^2 + \hbar^2\frac{k_x^2 + k_y^2}{2m_t}$$

$$\pm \left(\frac{\pi n}{k_0 t}\right)^2 \frac{|D\varepsilon_{xy} - \frac{\hbar^2 k_x k_y}{M}|}{k_0 t|1 - (\pi n/k_0 t)^2|}\sin(k_0 t). \quad (17)$$

It immediately follows that the subband degeneracy is preserved only in the absence of shear strain, and when and either $k_x = 0$ or $k_y = 0$. Equation (17) demonstrates that in thin films the unprimed subbands are *not equivalent* even without shear strain. Dispersion (17) also predicts different effective masses in [110] direction for the unprimed subbands with the same quantum number n without strain

$$m_{(1,2)} = \left(\frac{1}{m_t} \pm \frac{1}{M} \left(\frac{\pi n}{k_0 t} \right)^2 \frac{\sin(k_0 t)}{k_0 t |1 - (\pi n / k_0 t)^2|} \right)^{-1}. \quad (18)$$

This explains the difference between the masses found numerically for the two ground subbands in relaxed films presented in Fig. 3b.

6.4 Subband splitting

Although the splitting between the heavy and light hole subbands is known to depend on the film thickness and the stress value, leading to a radical change of the electrical and optical properties of the system [60], the unprimed subbands in (001) inversion layers and thin films are degenerate within the effective mass approximation [38]. We now analyze the splitting in energy between the two unprimed subbands with the same n, which is usually called the valley splitting [61], as it follows from (8), (10), and (17).

6.4.1 Valley splitting in magnetic field

For zero shear strain the Landau levels in an orthogonal magnetic field B are found from (17) by using the Bohr-Sommerfeld quantization conditions:

$$E_m^{(1,2)} = \hbar \omega_c \left(m + \frac{1}{2} \right) \frac{\pi}{4 \arctan(\sqrt{m_{(1,2)}/m_{(2,1)}})}, \quad (19)$$

where the masses are determined by (18), and

$$\omega_c = \frac{eB}{\sqrt{m_1 m_2} c}$$

is the cyclotron frequency, e is the electron charge, and c is the speed of light. According to (19), the difference $|E_m^1 - E_m^2|$ is linear regarding the magnetic field.

In Shubnikov-de-Haas experiments there will now occur two sets of resistance oscillations with slightly different periods in inverse magnetic field. Because of the small difference between the masses the difference in the periods will also be small. However, at the Fermi level the quantum number m, which is proportional to the ratio of the Fermi energy to the cyclotron frequency, is typically very large and may lead to a splitting of several hundreds μeV. The difference in the periods can be interpreted as an appearance of an additional energy shift between the equivalent unprimed valleys. Most importantly, the shift is linear in the magnetic field.

The linear dependence of splitting between the valleys on the magnetic field will be also observed even in the presence of a small intrinsic constant valley splitting as long as this splitting is much smaller than the Fermi energy. This splitting is possible due to a remaining shear strain and/or conduction band non-parabolicity which is not accounted for in the two-band k·p theory and is usually several tens of μeV, thus much smaller than the Fermi energy. For a 10 nm thick silicon film grown on SiGe it follows from (19) that the valley splitting can be several tens μeVs in a magnetic field of 1 T, which is consistent with the experimental observations [61].

6.4.2 Valley splitting in a point contact

We consider a point contact in [110] direction realized by confining an electron system of a thin silicon film laterally by depleting the area under additional gates. Without strain the low-energy effective Hamiltonian in the point contact can be written as:

$$H_{(1,2)} = \frac{\hbar^2 k_x'^2}{2m_{(2,1)}} + \frac{\hbar^2 k_y'^2}{2m_{(1,2)}} + \frac{1}{2} \kappa x'^2 + V_b, \quad (20)$$

where the primed variables are along the [110] and [1-10] axes, the effective masses are determined by (18), κ is the spring constant of the point contact confinement potential $V(x') = \kappa x'^2/2$ in [1-10] direction, and V_b is a gate voltage dependent conduction band shift in the point contact [62]. The dispersion relation of propagating modes within the point contact is written as:

$$E_p^{(1,2)} = \frac{k^2 k_x'^2}{2m_{(2,1)}} + \hbar \omega_{(1,2)} \left(p + \frac{1}{2} \right) + V_b, \quad (21)$$

where $\omega_{(1,2)}^2 = \kappa / m_{(1,2)}$. Since the energy minima of the two propagating modes with the same p are separated, they are resolved in the conductance experiment through the point contact as two distinct steps. The valley splitting is $\Delta E_p = \hbar |\omega_1 - \omega_2|$. The difference in the effective masses (18) and, correspondingly, the valley splitting can be greatly enhanced by reducing the effective thickness t of the quasi-two-dimensional electron gas, which is usually the case in a gated electron system, when the inversion layer is formed.

In a [100] oriented point contact without strain the effective Hamiltonian is

$$H^{\pm} = \hbar^2 \frac{k_x^2 + k_y^2}{2m_t} \pm \left(\frac{\pi n}{k_0 t} \right)^2 \frac{|\frac{\hbar^2 k_x k_y}{M}| \sin(k_0 t)}{k_0 t |1 - (\pi n / k_0 t)^2|} + \frac{\kappa}{2} x^2.$$

Due to symmetry with respect to k_y the subband minima in a point contact are always degenerate. For this reason the valley splitting in [100] oriented point contacts is greatly reduced.
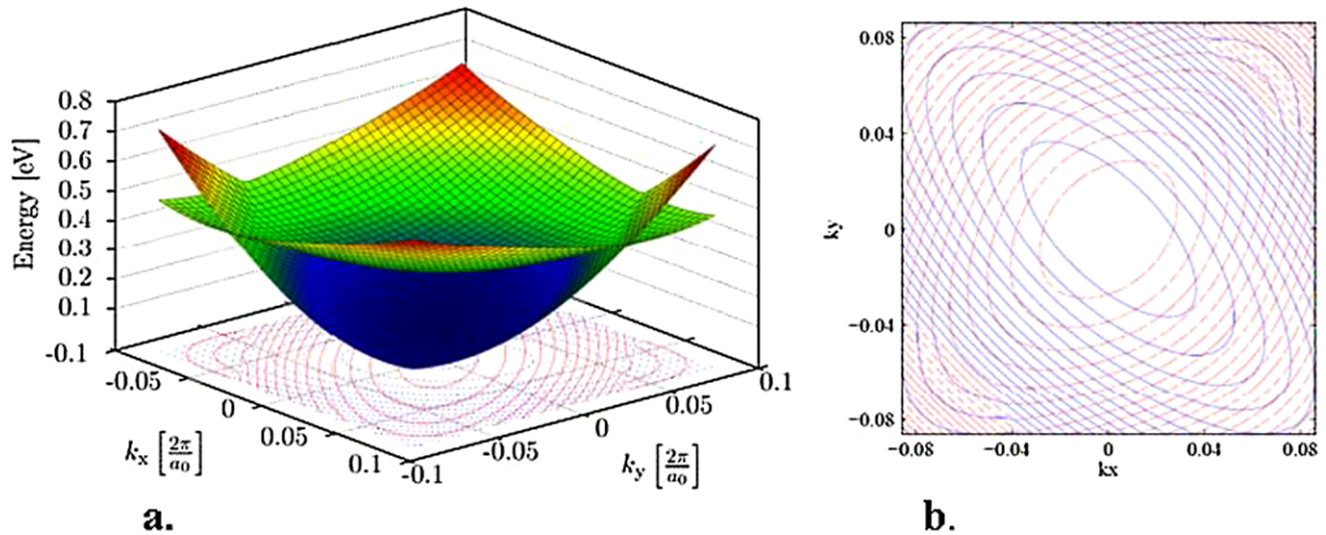
Fig. 5 Dispersions of the two ground subbands for a strained film thickness of 1.36 nm: **a**. Shear strain of 1% removes the degeneracy between the minima of the ground subbands shown in Fig. 4a. The subband dispersions are now characterized by the corresponding effective masses in [110] and [1-10] direction. **b**. The contour plot of Fig. 5a
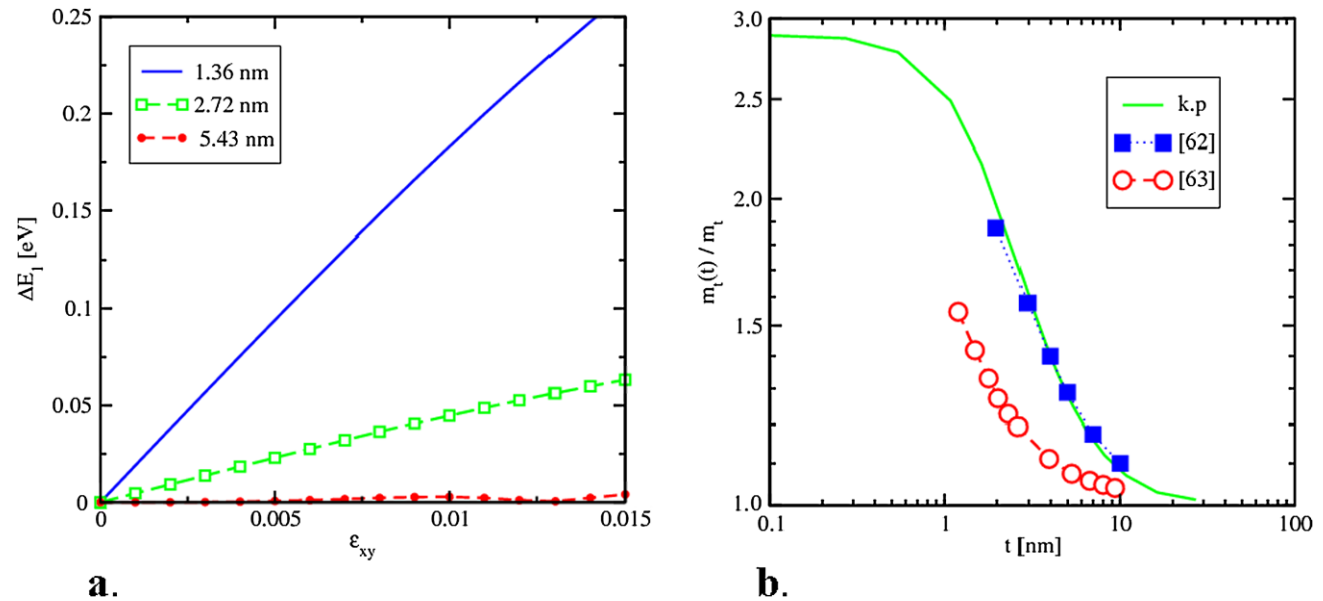

Fig. 6 **a**. Shear strain induced splitting of the ground subbands for several film thicknesses. In ultra-thin films the splitting is larger than kT already for moderate stress. **b**. The thickness dependence of the effective mass of the lowest primed subbands computed with the two-band k·p model (*solid line*) is in excellent agreement with the full-band calculations [65] (*filled symbols*). *Open symbols* show calculations from [66]

6.4.3 Valley splitting by shear strain

It follows from (17) that shear strain induces a valley splitting linear in strain for small shear strain values [59]:

$$\Delta E_n = 2\left(\frac{\pi n}{k_0 t}\right)^2 \frac{D\varepsilon_{xy}}{k_0 t |1 - (\pi n / k_0 t)^2|} \sin(k_0 t). \qquad (22)$$

The valley splitting is inversely proportional to $(k_0 t)^3$ and oscillates with the film thickness, in agreement with earlier work [38, 63].

One can also evaluate the maximum subband splitting achieved in the limit $\eta \to \infty$. In this limit it follows from (2) that the band dispersion becomes parabolic again around the minimum located exactly at the X-point. The subband quantization energies are thus determined by the usual quantiza-
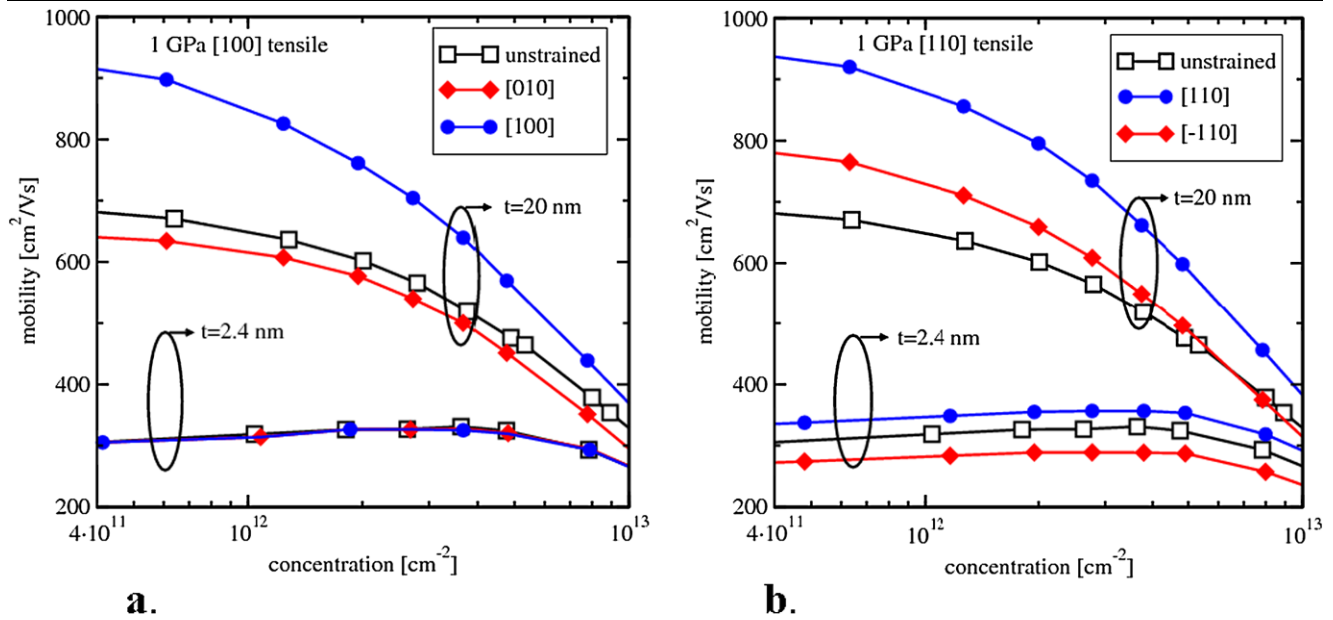
a.

b.

Fig. 7 a. The mobility enhancement in [100] direction due to [100] tensile stress of 1 GPa is due to de-population of the primed subbands with an unfavourable effective mass in transport direction. In ultra-thin films, where the primed subbands are already de-populated, the mo-

bility remains unchanged. **b**. The mobility enhancement due to tensile stress of 1 GPa in [110] transport direction is preserved even in ultra-thin films due to the transport mass decrease

tion conditions, which results in the subband splitting

$$\Delta E_n = \left(\frac{\hbar\pi}{t} \right)^2 \frac{2n-1}{2m_t}. \tag{23}$$

For practically relevant intermediate strain values a numerical solution is required. Figure 5 demonstrates the energy dispersion for the two ground subbands in a thin film with 1% shear strain. Splitting between the subbands becomes apparent. Results of calculations of the splitting between the ground subbands are shown in Fig. 6a. It demonstrates that the valley splitting can be effectively controlled by adjusting the shear strain and modifying the effective thickness t of the electron system. For extremely high strain values, when the dispersion of the lowest conduction band becomes parabolic again, the quantization levels in a square well potential (23) are recovered. Although the value of strain in this limit is unrealistic, this result is used to analyze dispersion relations for the primed subbands.

Uniaxial stress along [110] channel direction, which induces shear strain, is already used by industry to enhance the performance of modern MOSFETs. Therefore, its application to control valley splitting does not require expensive technological modifications. A possibility to introduce a valley splitting larger than the Zeeman spin splitting makes silicon promising for future spintronic applications [61].

As seen from Fig. 6a, the valley splitting in ultra-thin films can be quite large already for reasonable stress val-

ues. In this case the higher subband becomes de-populated, prompting for a mobility enhancement in (001) ultra-thin films strained along [110] direction.

6.5 Effective mass of primed subbands

Shear strain in [110] direction does not affect the primed valleys along [100] and [010] direction, except for a small shift of the minimum [64]. However, recent calculations of the primed subbands based on the density functional theory (DFT) [65] and the "linear combination of bulk bands" method obtained with the empirical pseudo-potential calculations [66] reveal the dependence of the transport effective masses on silicon film thickness t. Here we briefly analyze the effective mass of the primed subbands based on the two-band Hamiltonian (1). We assume the quantization direction along the [100] axis. By formally replacing k_0/m_l with k_y/M and $k_x k_y/M$ with $k_z k_0/m_l$ in (1) one finds the dispersion relation and the effective masses in the primed subbands, where results of calculations are shown in Fig. 6b. The two-band k·p results are in excellent agreement with the results of the "linear combination of the bulk bands" method with a potential barrier of 3 eV at the film interface [66], and they are also consistent with the DFT calculations [65].

7 Electron transport in uniaxially stressed films

7.1 Mobility enhancement

A multi-subband Monte Carlo method designed for small signal analysis [67] was used to evaluate the mobility in MOSFETs with a thin silicon film. The method is based on the solution of the linearized multi-subband Boltzmann equation, which is exact in the limit of vanishing driving fields. A particular advantage of the method is that it includes degeneracy effects due to the Pauli exclusion principle. Degeneracy effects are important for mobility calculations in ultra-thin films, especially at high carrier concentrations. The multi-subband method uses the subband wave functions and subband energies. They can be found by solving the Schrödinger equation and the Poisson equation self-consistently for each value of the gate voltage. The wave functions are then employed to evaluate the scattering rates. Scattering with phonons and surface roughness is included. The surface roughness at the two thin film interfaces is assumed to be equal and uncorrelated. The parameters of the Gaussian surface roughness correlation function were calibrated to reproduce the universal mobility curve of Takagi [68] in the inversion layer. The same parameters are then used for the mobility calculations in thin film MOSFETs.

Figure 7a shows the mobility in (001) silicon films for two film thicknesses under tensile uniaxial stress of 1 GPa in [100] direction. The stress shifts up and de-populates the two [100] primed valleys with unfavorable mass m_l in the transport direction providing the mobility enhancement in the stress direction for a 20 nm film. In [010] transport direction the [100] primed valleys have a smaller transversal mass. Therefore, the de-population of the [100] primed subbands due to [100] tensile stress has a detrimental effect on the mobility in [010] direction. In ultra-thin films the primed subbands are nearly de-populated already without stress due to the large separation in energy between primed and unprimed subbands in a silicon film with a thickness of 2.4 nm. Therefore, additional shifting up in energy of the [100] valleys does not have any effect on the mobility in ultra-thin films (Fig. 7a).

Apart from shifting the primed subbands with unfavorable transport masses in the (001) plane up in energy and de-populating them, tensile stress in [110] direction generates a shear component which modifies the transport effective masses of the unprimed subbands (Fig. 4b). The decrease of the effective masses in [110] direction induced by shear strain becomes more pronounced with the film thickness reduced guaranteeing the mobility enhancement even in ultra-thin films, as demonstrated in Fig. 7b. However, the density of states effective mass in unprimed subbands increases with shear strain. This results in higher scattering rates which

deteriorate the benefits of the thickness-enhanced transport mass decrease at higher stress values, as displayed in Fig. 7b, although the mobility enhancement remains substantial.

7.2 Current enhancement in ultimate MOSFETs

Calculated subband parameters are used to evaluate transport in a ballistic MOSFET [69], which is sometimes considered as the ultimate limit of scaling [70]. Although backscattering [71] cannot be completely ignored in modern devices, they already operate at approximately 70% of ballisticity. It is thus expected that with scaling continuing the next generation MOSFETs would operate even closer to the ballistic limit. Therefore, the results below demonstrate the upper estimate on how effective strain can be for current enhancement for ultra-scaled MOSFETs provided the ballistic limit will be achieved.

We follow the Natori approach [69] in which the current along the [110] direction is determined by:

$$I/W = \frac{e\sqrt{2}(kT)^{3/2}}{\pi^2\hbar^2} \sum_n \sqrt{m_{ny}} \left\{ F_{1/2}\left[\frac{E_F - E_n}{kT}\right] - F_{1/2}\left[\frac{E_F - E_n - eV_{DS}}{kT}\right] \right\} \quad (24)$$

where

$$F_{1/2}[x] = \int_0^\infty dz \frac{\sqrt{z}}{1 + \exp(x - z)}$$

is the Fermi-Dirac integral, E_F is the source chemical potential, V_{DS} is the source-drain voltage, and E_n and m_{ny} are the subband energies and the subband effective masses in the direction orthogonal to the current.

The two-dimensional charge concentration N_s in the channel is determined by the following expression [69]:

$$N_s = \frac{kT}{2\pi\hbar^2} \sum_n \sqrt{m_{ny}m_{nx}} \left\{ \ln\left[1 + \exp\frac{E_F - E_n}{kT}\right] - \ln\left[1 + \exp\frac{E_F - E_n - eV_{DS}}{kT}\right] \right\}. \quad (25)$$

The charge concentration determines the gate voltage V_G as:

$$eV_G = C_{\text{eff}}^{-1} eN_s + (E_F - E_1), \quad (26)$$

where $C_{\text{eff}}^{-1} = 2\pi[t_{ox}/\varepsilon_{ox} + t_s/\varepsilon_s\{1/6 + 5/(2\pi^2)\}]$ is the inverse capacitance of a double-gate structure.

For the thick film the effective masses closely follow the analytical expressions (16) obtained by neglecting the valley coupling. For higher shear strain values one starts to observe deviations from (16) due to an increased coupling between the valleys (Fig. 2a). The effect of the valley interaction is more pronounced in thin films as shown
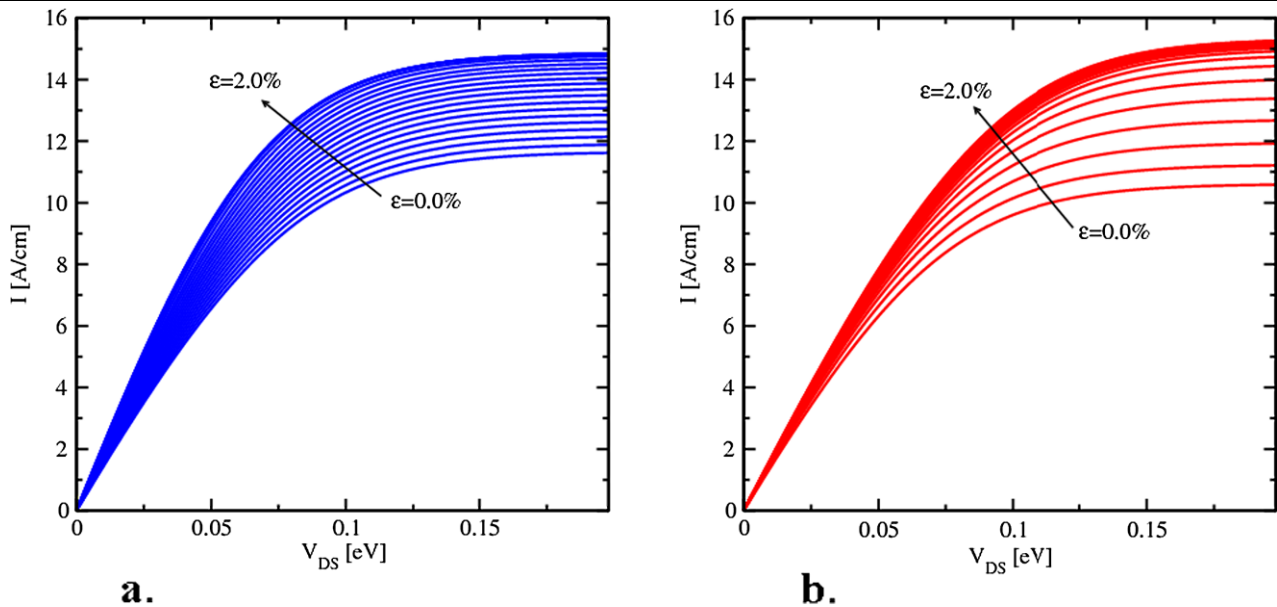
Fig. 8 a. The *IV* characteristics of a double-gate ballistic MOSFET with a silicon body of 10.86 nm thickness as function of shear strain at $V_G = 0.5$ V. Strain is increased from 0 to 2% in steps of 0.1%. **b**. The same as in Fig. 8a but for a body thickness $t = 1.36$ nm

in Fig. 2b. The valley coupling caused by strain and reduced thickness introduces a substantial difference in the effective masses of the two unprimed subbands with the same quantum number, which are usually treated as completely equivalent. Even more, a clear difference in masses is already observed in unstrained films of $t = 2.7$ nm visible in Fig. 3b, which becomes high in an ultra-thin film with the thickness $t = 1.4$ nm.

We have used these subband parameters for calculations of *IV* characteristics. Examples of the *IV*s for $t = 10.86$ nm and $t = 1.4$ nm at the gate voltage V_G after (26) are shown in Figs. 8a and 8b, correspondingly.

An enhancement of the drive current with shear strain for all V_{DS} is observed. In order to characterize the enhancement quantitatively, we have evaluated the relative current increase as $(I(V_{DS}) - I_0(V_{DS}))/I_0(V_{DS})$ for each value of the source-drain voltage. Results for different film thicknesses are shown in Fig. 9.

For small shear strain values the current enhancement is bias independent for all studied film thicknesses. For high strain the saturation of the current enhancement is observed. For intermediate strain values the enhancement behaves differently in thick and thin silicon films at high and low voltages.

In thicker films the enhancement in the linear regime is larger than in saturation. Figure 9a shows the current increase with the exact values from Fig. 2a for the effective masses and with the masses (16), which demonstrates that the enhancement in a $t = 10.86$ nm film is due to the effective mass modifications with strain. For small strain values the current enhancement is due to the m_y increase. How-

ever, for larger strain the density-of-states effective mass $(m_x m_y)^{1/2}$ starts increasing. For fixed gate voltage it lowers the chemical potential E_F, thus reducing the current.

At saturation only a half of the states flowing from source to drain is filled. For a fixed gate voltage it results in a higher chemical potential compared to the linear current regime, where the difference in states filling flowing from source to drain and in opposite direction is small. The decrease of E_F due to the strain-induced increase in the density-of-states is thus more pronounced in saturation leading to a substantially smaller current enhancement.

In thin silicon films the behavior of the enhancement is reversed (Fig. 9b). This cannot be explained by the change in the subband effective masses alone. The main reason is the strain-induced energy splitting between the unprimed subbands with the same quantum number. The splitting increases with strain and is particularly large in thin films. Because of this splitting the density of states decreases with strain prompting an increase in the chemical potential and current. In saturation the increase of E_F is larger than in the linear regime, which guarantees the large drive current enhancement.

8 Conclusion

A rigorous analysis of the subband structure in thin silicon films is performed. The thickness dependence of the effective mass of primed subbands calculated within the two-band k·p model is in agreement with earlier full-band calculations. It is demonstrated that within the two-band
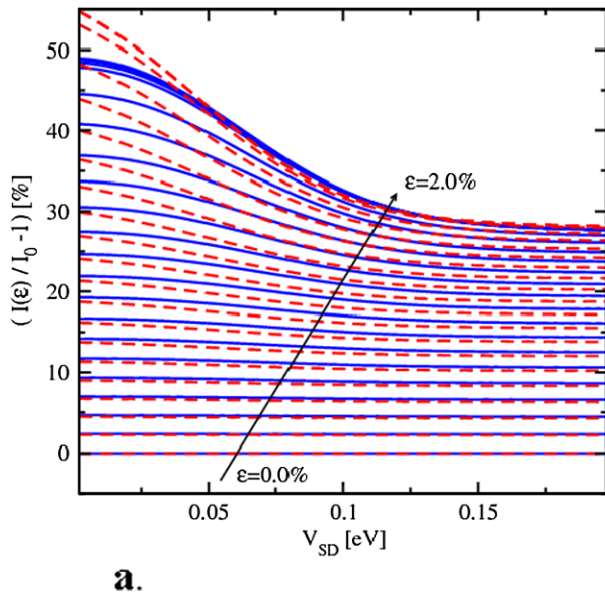
Fig. 9 a. Current enhancement as a function of drain bias for several shear strain values for a ballistic MOSFET with a silicon body thickness $t = 10.86$ nm. The enhancement is mostly due to the effective mass modification (1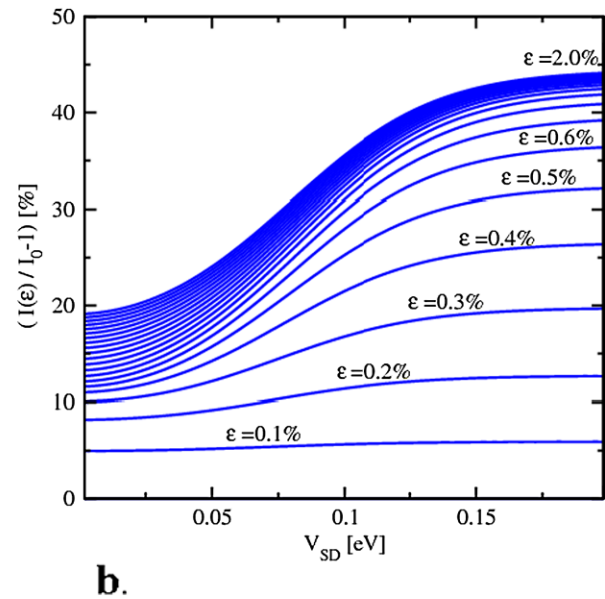6) as indicated by *dashed lines*. **b.** The same as in Fig. 8a but for a body thickness $t = 1.36$ nm. The enhancement of the on-current at saturation is larger due to an additional strain-induced splitting between the unprimed subbands shown in Fig. 6a

k·p model the unprimed subbands with the same quantum number n are not equivalent. A large splitting between the unprimed valleys of ultra-thin films can be introduced by a shear strain component. Calculated subband effective masses are shown to depend on shear strain and thickness simultaneously. Interestingly, the effective masses of the two unprimed valleys are different in ultra-thin silicon films even without strain. This results in a linear dependence of the subband splitting on the magnetic field strength and leads to large subband splitting in a laterally confined electron system in a point contact.

The mobility enhancement in strained MOSFETs with ultra-thin silicon films is investigated by a subband Monte Carlo method. The method based on the solution of the linearized Boltzmann equation accounts for the carrier degeneracy exactly. Transport in thin films is determined by the subband structure, in particular by the effective masses. The decrease of the transport effective mass and additional splitting between the unprimed subbands induced by the shear strain component is the reason for current enhancement even in ultra-thin (001) silicon films. This mobility and drive current increase combined with the improved channel control makes multi-gate MOSFETs based on thin films or silicon fins preeminent candidates for the 22 nm technology node and beyond.

References

1. Doris, B., Ieong, M., Kanarsky, T., Zhang, Y., Roy, R.A., Documaci, O., Ren, Z., Jamin, F.-F., Shi, L., Natzle, W., Huang, H.-J., Mezzapelle, J., Mocuta, A., Womack, S., Gribelyuk, M., Jones, E.C., Miller, R.J., Wong, H.-S.P., Haensch, W.: Extreme scaling with ultra-thin Si channel MOSFETs. In: IEDM Tech. Dig., pp. 267–270 (2002)
2. Natarajan, S., Armstrong, M., Bost, M., Brain, R., Brazier, M., Chang, C., Chikarmane, V., Childs, M., Deshpande, H., Dev, K., Ding, G., Ghani, T., Golonzka, O., Han, W., He, J., Heussner, R., James, R., Jin, I., Kenyon, C., Klopcic, S., Lee, S., Liu, M., Lodha, S., McFadden, B., Murthy, A., Neiberg, L., Neirynck, J., Packan, P., Pae, S., Parker, C., Pelto, C., Pipes, L., Sebastian, J., Seiple, J., Sell, B., Sivakumar, S., Song, B., Tone, K., Troeger, T., Weber, C., Yang, M., Yeoh, A., Zhang, K.: A 32 nm logic technology featuring 2nd-generation high-k + metal-gate transistors, enhanced channel strain and 0.171 μm² SRAM cell size in a 291 Mb array. In: IEDM Tech. Dig., pp. 941–943 (2008)
3. Mistry, K., Allen, C., Auth, C., Beattie, B., Bergstrom, D., Bost, M., Brazier, M., Buehler, M., Cappellani, A., Chau, R., Choi, C., Ding, G., Fischer, K., Ghani, T., Grover, R., Han, W., Hanken, D., Hattendorf, M., He, J., Hicks, J., Huessner, R., Ingerly, D., Jain, P., James, R., Jong, L., Joshi, S., Kenyon, C., Kuhn, K., Lee, K., Liu, H., Maiz, J., McIntyre, B., Moon, P., Neirynck, J., Pae, S., Parker, C., Parsons, D., Prasad, C., Pipes, L., Prince, M., Rarade, P., Reynolds, T., Sandford, J., Shifren, L., Sebastian, J., Seiple, J., Simon, D., Sivakumar, S., Smith, P., Thomas, C., Troeger, T., Vandervoorn, P., Williams, S., Zawadzki, K.: A 45 nm logic technology with high-k+metal gate transistors, strained silicon, 9 Cu interconnect layers, 193 nm dry patterning, and 100% Pb-free packaging. In: IEDM Tech. Dig., pp. 247–250 (2007)
4. Hudait, M.K., Dewey, G., Datta, S., Fastenau, J.M., Kavalieros, J., Liu, W.K., Lubyshev, D., Pillarisetty, R., Rachmady, W., Radosavljevic, M., Rakshit, T., Chau, R.: Heterogeneous integration of enhancement mode in 0.7 Ga 0.3 As quantum well transistor

on silicon substrate using thin (≤2 μm) composite buffer architecture for high-speed and low-voltage (0.5 V) logic applications. In: IEDM Tech. Dig., pp. 625–628 (2007)

5. Chau, R.: Challenges and opportunities of emerging nanotechnology for future VLSI nanoelectronics. In: Rec. International Semiconductor Device Research Symposium (ISDRS), p. 3 (2007)

6. Hall, H.H., Bardeen, J., Pearson, G.L.: The effects of pressure and temperature on the resistance of p–n junctions in germanium. Phys. Rev. **84**(1), 129–132 (1951)

7. Smith, C.S.: Piezoresistance effect in germanium and silicon. Phys. Rev. **94**(1), 42–49 (1954)

8. Fitzgerald, E.A., Xie, Y.H., Green, M.L., Brasen, D., Kortan, A.R., Michel, J., Mii, Y.J., Weir, B.: Totally relaxed Ge$_x$Si$_{1-x}$ layers with low threading dislocation densities grown on Si substrates. Appl. Phys. Lett. **59**(7), 811–813 (1991)

9. Welser, J., Hoyt, J.L., Gibbons, J.F.: NMOS and PMOS transistors fabricated in strained silicon/relaxed silicon-germanium structures. In: IEDM Tech. Dig., pp. 1000–1002 (1992)

10. Welser, J., Hoyt, J.L., Gibbons, J.F.: Electron mobility enhancement in strained-Si n-type metal-oxide-semiconductor field-effect transistors. IEEE Electron Device Lett. **15**(3), 100–102 (1994)

11. Ghyselen, B., Hartmann, J.M., Ernst, T., Aulnette, C., Osternaud, B., Bogumilowicz, Y., Abbadie, A., Besson, P., Rayssac, O., Tiberj, A.: Engineering strained silicon on insulator wafers with the smart CutTM technology. Solid-State Electron. **48**(8), 1285–1296 (2004)

12. Sadaka, M., Thean, A.V.Y., Barr, A., Tekleab, D., Kalpat, S., White, T.: Fabrication and operation of sub-50 nm strained-Si on Si$_{1-x}$Ge$_x$ on insulator (SGOI) CMOSFETs. In: IEEE International SOI Conference, pp. 209–211 (2004)

13. Rim, K., Chan, K., Shi, L., Boyd, D., Ott, J., Klymko, N., Cardone, F., Tai, L., Koester, S., Cobb, M., Canaperi, D., To, B., Duch, E., Babich, I., Carruthers, R., Saunders, P., Walker, G., Zhang, Y., Steen, M., Ieong, M.: Fabrication and mobility characteristics of ultra-thin strained Si directly on insulator (SSDOI) MOSFETs. In: IEDM Tech. Dig., pp. 49–52 (2003)

14. Andrieu, F., Ernst, T., Faynot, O., Rozeau, O., Bogumilowicz, Y., Hartmann, J.M., Brevard, L., Toffoli, A., Lafond, D., Ghyselen, B.: Performance and physics of sub-50 nm strained Si on Si$_{1-x}$Ge$_x$ on insulator (SGOI) nMOSFETs. Solid-State Electron. **50**(4), 566–572 (2006)

15. Wang, E.X., Matagne, P., Shifren, L., Obradovic, B., Kotlyar, R., Cea, S., Stettler, M., Giles, M.D.: Physics of hole transport in strained silicon MOSFET inversion layers. IEEE Trans. Electron Devices **53**(8), 1840–1851 (2006)

16. Sun, G., Sun, Y., Nishida, T., Thompson, S.E.: Hole mobility in silicon inversion layers: stress and surface orientation. J. Appl. Phys. **102**(8), 084501 (2007)

17. Fischetti, M.V., Laux, S.E.: Band structure, deformation potentials, and carrier mobility in Si, Ge, and SiGe alloys. J. Appl. Phys. **80**(4), 2234–2252 (1996)

18. Scott, G., Lutze, J., Rubin, M., Nouri, F., Manley, M.: NMOS drive current reduction caused by transistor layout and trench isolation induced stress. In: IEDM Tech. Dig., pp. 827–830 (1999)

19. Matsumoto, T., Maeda, S., Dang, H., Uchida, T., Ota, K., Hirano, Y., Sayama, H., Iwamatsu, T., Ipposhi, T., Oda, H., Maegawa, S., Inoue, Y., Nishmura, T.: Novel SOI wafer engineering using low stress and high mobility CMOSFET with ⟨100⟩ channel for embedded RF/analog applications. In: IEDM Tech. Dig., pp. 663–666 (2002)

20. Steegen, A., Stucchi, M., Lauwers, A., Maex, K.: Silicide induced pattern density and orientation dependent transconductance in MOS transistors. In: IEDM Tech. Dig., pp. 497–500 (1999)

21. Ito, S., Namba, H., Yamaguchi, K., Hirata, T., Ando, K., Koyama, S., Kuroki, S., Ikezawa, N., Suzuki, T., Saitoh, T., Horiuchi, T.: Mechanical stress effect of etch-stop nitride and its impact on deep submicron transistor design. In: IEDM Tech. Dig., pp. 247–251 (2002)

22. Shimizu, A., Hachimine, K., Ohki, N., Ohta, H., Koguchi, M., Nonaka, Y., Sato, H., Ootsuka, F.: Local mechanical-stress control (LMC): a new technique for CMOS-performance enhancement. In: IEDM Tech. Dig., pp. 433–436 (2001)

23. Ouyang, Q., Yang, M., Holt, J., Panda, S., Chen, H., Utomo, H., Fischetti, M., Rovedo, N., Jinghong, L., Klymko, N., Wildman, H., Kanarsky, T., Costrini, G., Fried, D.M., Bryant, A., Ott, J.A., Ieong, M., Sung, C.-Y.: Investigation of CMOS devices with embedded SiGe source/drain on hybrid orientation substrates. In: Int. Symp. on VLSI Technology, pp. 28–29 (2005)

24. Bai, P., Auth, C., Balakrishnan, S., Bost, M., Brain, R., Chikarmane, V., Heussner, R., Hussein, M., Hwang, J., Ingerly, D., James, R., Jeong, J., Kenyon, C., Lee, E., Lee, S.H., Lindert, N., Liu, M., Ma, Z., Marieb, T., Murthy, A., Nagisetty, R., Natarajan, S., Neirynck, J., Ott, A., Parker, C., Sebastian, J., Shaheed, R., Sivakumar, S., Steigerwald, J., Tyagi, S., Weber, C., Woolery, B., Yeoh, A., Zhang, K., Bohr, M.: A 65 nm logic technology featuring 35 nm gate lengths, enhanced channel strain, 8 Cu interconnect layers, low-k ILD and 0.57 μm^2 SRAM cell. In: IEDM Tech. Dig., pp. 657–660 (2004)

25. Ang, K.-W., Chui, K.J., Bliznetsov, V., Du, A., Balasubramanian, N., Li, M.F., Samudra, G., Yeo, Y.C.: Enhanced performance in 50 nm n-MOSFETs with silicon-carbon source/drain regions. In: IEDM Tech. Dig., pp. 1069–1071 (2004)

26. Ang, K.-W., Chui, K.J., Bliznetsov, V., Tung, C.H., Du, A., Balasubramanian, N., Samudra, G., Li, M.F., Yeo, Y.C.: Lattice strain analysis of transistor structures with silicon–germanium and silicon–carbon source/drain stressors. Appl. Phys. Lett. **86**(3), 093102 (2005)

27. Pidin, S., Mori, T., Inoue, K., Fukuta, S., Itoh, N., Mutoh, E., Ohkoshi, K., Nakamura, R., Kobayashi, K., Kawamura, K., Saiki, T., Fukuyama, S., Satoh, S., Kase, M., Hashimoto, K.: A novel strain enhanced CMOS architecture using selectively deposited high tensile and high compressive silicon nitride films. In: IEDM Tech. Dig., pp. 213–216 (2004)

28. Sheraw, C.D., Yang, M., Fried, D.M., Costrini, G., Kanarsky, T., Lee, W.H., Chan, V., Fischetti, M.V., Holt, J., Black, L., Naeem, M., Panda, S., Economikos, L., Groschopf, J., Kapur, A., Li, Y., Mo, R.T., Bonnoit, A., Degraw, D., Luning, S., Chidambarrao, D., Wang, X., Bryant, A., Brown, D., Sung, C.Y., Agnello, P., Ieong, M., Huang, S.F., Chen, X., Khare, M.: Dual stress liner enhancement in hybrid orientation technology. In: Int. Symp. on VLSI Technology, pp. 12–13 (2005)

29. Arghavani, R., Xia, L., Saad, H.M., Balseanu, M., Karunasiri, G., Mascarenhas, A., Thompson, S.E.: A reliable and manufacturable method to induce a stress of >1 GPa on a p-channel MOSFET in high volume manufacturing. IEEE Electron Device Lett. **27**(2), 114–116 (2006)

30. Jan, C.H., Bai, P., Choi, J., Curello, G., Jacobs, S., Jeong, J., Johnson, K., Jones, D., Klopcic, S., Lin, J., Lindert, N., Lio, A., Natarajan, S., Neirynck, J., Packan, P., Park, J., Post, I., Patel, M., Ramey, S., Reese, P., Rockford, L., Roskowski, A., Sacks, G., Turkot, B., Wang, Y., Wei, L., Yip, J., Young, I., Zhang, K., Zhang, Y., Bohr, M., Holt, B.: A 65 nm ultra low power logic platform technology using uni-axial strained silicon transistors. In: IEDM Tech. Dig., pp. 60–63 (2005)

31. Horstmann, M., Wei, A., Kammler, T., Höntschel, J., Bierstedt, H., Feudel, T., Frohberg, K., Gerhardt, M., Hellmich, A., Hempel, K., Hohage, J., Javorka, P., Klais, J., Koerner, G., Lenski, M., Neu, A., Otterbach, R., Press, P., Reichel, C., Trentsch, M., Trui, B., Salz, H., Schaller, M., Engelmann, H.J., Herzog, O., Ruelke, H., Hübler, P., Stephan, R., Greenlaw, D., Raab, M., Kepler, N.: Integration and optimization of embedded-SiGe, compressive and tensile stressed liner films, and stress memorization in advanced SOI CMOS technologies. In: IEDM Tech. Dig., pp. 233–236 (2005)

32. Luttinger, J.M., Kohn, W.: Motion of electrons and holes in perturbed periodic fields. Phys. Rev. **97**(4), 869–883 (1955)

33. Bir, G.L., Pikus, G.E.: Symmetry and Strain-Induced Effects in Semiconductors. Wiley, New York (1974)

34. Sun, Y., Thompson, S.E., Nishida, T.: Physics of strain effects in semiconductors and metal-oxide-semiconductor field-effect transistors. J. Appl. Phys. **101**, 104503 (2007)

35. Fischetti, M.V., Ren, Z., Solomon, P.M., Yang, M., Rim, K.: Six-band k·p calculation of the hole mobility in silicon inversion layers: dependence on surface orientation, strain, and silicon thickness. J. Appl. Phys. **94**(2), 1079–1095 (2003)

36. Sato, T., Takeishi, Y., Hara, H.: Effects of crystallographic orientation on mobility, surface state density, and noise in p-type inversion layers on oxidized silicon surfaces. Jpn. J. Appl. Phys. **8**, 588 (1969)

37. Pham, A.T., Jungemann, C., Meinerzhagen, B.: Deterministic multisubband device simulations for strained double gate PMOS-FETs including magnetotransport. In: IEDM Tech. Dig., pp. 895–898 (2008)

38. Ando, T., Fowler, A.B., Stern, F.: Electronic properties of two-dimensional systems. Rev. Mod. Phys. **54**(2), 437–672 (1982)

39. Rieger, M., Vogl, P.: Electronic-band parameters in strained $Si_{1-x}Ge_x$ alloys on $Si_{1-y}Ge_y$ substrates. Phys. Rev. B **48**(19), 14276–14287 (1993)

40. Fischetti, M.V., Gámiz, F., Hänsch, W.: On the enhanced electron mobility in strained-silicon inversion layers. J. Appl. Phys. **92**(12), 7320–7324 (2002)

41. Takagi, S.I., Hoyt, J.L., Welser, J.J., Gibbons, J.F.: Comparative study of phonon-limited mobility of two-dimensional electrons in strained and unstrained Si metal-oxide-semiconductor field-effect transistors. J. Appl. Phys. **80**(3), 1567–1577 (1996)

42. Uchida, K., Krishnamohan, T., Saraswat, K.C., Nish, Y.: Physical mechanisms of electron mobility enhancement in uniaxial stressed MOSFETs and impact of uniaxial stress engineering in ballistic regime. In: IEDM Tech. Dig., pp. 129–132 (2005)

43. Uchida, K., Kinoshita, A., Saitoh, M.: Carrier transport in (110) nMOSFETs: subband structure, non-parabolicity, mobility characteristics, and uniaxial stress engineering. In: IEDM Tech. Dig., pp. 1019–1021 (2006)

44. Esseni, D., Palestri, P.: Linear combination of bulk bands method for investigating the low-dimensional electron gas in nanostructured devices. Phys. Rev. B **72**(16), 165342 (2005)

45. Sverdlov, V., Esseni, D., Baumgartner, O., Kosina, H., Selberherr, S., Schanovsky, F., Esseni, D.: The linear combination of bulk bands-method for electron and hole subband calculations in strained silicon films and surface layers. In: Proc. IWCE, pp. 49–53 (2009)

46. Rideau, D., Feraille, M., Ciampolini, L., Minondo, M., Tavernier, C., Jaouen, H., Ghetti, A.: Strained Si, Ge, and $Si_{1-x}Ge_x$ alloys modeled with a first-principles-optimized full-zone k·p method. Phys. Rev. B **74**(19), 195208 (2006)

47. Hensel, J.C., Hasegawa, H., Nakayama, M.: Cyclotron resonance in uniaxially stressed silicon. II. Nature of the covalent bond. Phys. Rev. **138**(1A), A225–A238 (1965)

48. Ungersboeck, E., Dhar, S., Karlowatz, G., Sverdlov, V., Kosina, H., Selberherr, S.: The effect of general strain on band structure and electron mobility of silicon. IEEE Trans. Electron Devices **54**(9), 2183–2190 (2007)

49. Sverdlov, V., Ungersboeck, E., Kosina, H., Selberherr, S.: Effects of shear strain on the conduction band in silicon: an efficient two-band k·p theory. In: European Solid-State Device Research Conference (ESSDERC), pp. 386–389 (2007)

50. Sverdlov, V., Karlowatz, G., Dhar, S., Kosina, H., Selberherr, S.: Two-band k·p model for the conduction band in silicon: impact of strain and confinement on band structure and mobility. Solid State Electron. **52**, 1563–1568 (2008)

51. VASP (Vienna Ab-initio Simulation Program), Kresse, G., Hafner, J.: Phys. Rev. B **47**, 558 (1993)

52. VASP (Vienna Ab-initio Simulation Program), Kresse, G., Hafner, J.: Phys. Rev. B **49**, 14251 (1994)

53. VASP (Vienna Ab-initio Simulation Program), Kresse, G., Furth-müller, J.: Phys. Rev. B **54**, 11169 (1996)

54. VASP (Vienna Ab-initio Simulation Program), Kresse, G., Furth-müller, J.: Comput. Math. Sci. **6**, 15 (1996)

55. Boykin, T.B., Klimeck, G., Oyafuso, F.: Valence band effective-mass expressions in the $sp^3d^5s^*$ empirical tight-binding model applied to a Si and Ge parametrization. Phys. Rev. B **69**(11), 115201 (2004)

56. Niquet, Y.M., Lherbier, A., Persson, M.P., Triozon, F., Roche, S., Blasé, X., Rideau, D.: Atomistic tight-binding approaches to quantum transport. In: Proc. 13th International Workshop on Computational Electronics, pp. 293–296 (2009)

57. Niquet, Y.M., Rideau, D., Tavernier, C., Jaouen, H., Blase, X.: Model for the on-site matrix elements of the tight-binding Hamiltonian of a strained crystal: application to silicon, germanium and their alloys. Phys. Rev. B **79**, 245201-1–13 (2009)

58. Baumgartner, O., Karner, M., Sverdlov, V., Kosina, H.: Numerical quadrature of the subband distribution functions in strained silicon UTB devices. In: Proc. 13th International Workshop on Computational Electronics, pp. 53–56 (2009)

59. Sverdlov, V., Selberherr, S.: Electron subband structure and controlled valley splitting in silicon thin-body SOI FETs: two-band k·p theory and beyond. Solid State Electron. **52**(12), 1861–1866 (2008)

60. Kirchoefer, S.W., Holonyak, N.Jr., Hess, K., Meehan, K., Gulino, D.A., Drickamer, H.G., Coleman, J.J., Dapkus, P.D.: High pressure measurements on $Al_xGa_{1-x}As$-GaAs ($x = 0.5$ and 1) superlattices and quantum well heterostructure lasers. J. Appl. Phys. **53**, 6037–6042 (1982)

61. Goswami, S., Slinker, K.A., Friesen, M., McGuire, L.M., Truitt, J.L., Tahan, C., Klein, L.J., Chu, J.O., Mooney, P.M., van der Weide, D.W., Joynt, R., Coppersmith, S.N., Eriksson, M.A.: Controllable valley splitting in silicon quantum devices. Nat. Phys. **3**, 41–45 (2007)

62. van Wees, B.J., van Houten, H., Beenakker, C.W.J., Williamson, J.G., Kouwenhoven, L.P., van der Marel, D., Foxon, C.T.: Quantized conductance of point contacts in a two-dimensional electron gas. Phys. Rev. Lett. **60**(9), 848–850 (1988)

63. Friessen, M., Chutia, S., Tahan, C., Coppersmith, S.N.: Valley splitting theory of SiGe/Si/SiGe quantum wells. Phys. Rev. B **75**(11), 115318-1–12 (2007)

64. Rideau, D., Feraille, M., Michaillat, M., Niquet, Y.M., Tavernier, C., Jaouen, H.: On the validity of the effective mass approximation and the Luttinger k·p model in fully depleted SOI MOSFETs. Solid State Electron. **53**(4), 452–461 (2009)

65. Martinez, A., Kalna, K., Sushko, P.V., Shluger, A.L., Barker, J.R., Asenov, A.: Impact of body-thickness-dependent band structure on scaling of double-gate MOSFETs: a DFT/NEGF study. IEEE Trans. Nanotechnol. **8**(2), 159–166 (2009)

66. van der Steen, J.-L.P.J., Esseni, D., Palestri, P., Selmi, L., Hueting, R.J.E.: Validity of the parabolic effective mass approximation in silicon and germanium n-MOSFETs with different crystal orientations. IEEE Trans. Electron Devices **54**(8), 1843–1851 (2007)

67. Sverdlov, V., Ungersboeck, E., Kosina, H., Selberherr, S.: Volume inversion mobility in SOI MOSFETs for different thin body orientations. Solid State Electron. **51**(2), 299–305 (2007)

68. Takagi, S.-I., Toriumi, A., Iwase, M., Tango, H.: On the universality of inversion layer mobility in Si MOSFETs: part I—effects of substrate impurity concentration. IEEE Trans. Electron Devices **41**(12), 2357–2362 (1994)

69. Natori, K.: Ballistic metal-oxide-semiconductor field-effect transistor. J. Appl. Phys. **78**(8), 4879–4890 (1994)

70. Likharev, K.: Electronics below 10 nm. In: Nano and Giga Challenges in Electronics, pp. 27–68. Elsevier, Amsterdam (2003)

71. Lundstrom, M., Ren, Z.: Essential Physics of carrier transport in nanoscale MOSFETs. IEEE Trans. Electron Devices **49**(1), 133–141 (2002)